Editors' Suggestion

Magnetic Gradiometer for the Detection of Zero- to Ultralow-Field Nuclear Magnetic Resonance

Min Jiang,[1,2,3] Román Picazo Frutos,[2] Teng Wu,[2,*] John W. Blanchard,[2] Xinhua Peng,[1,3,4,†] and Dmitry Budker[2,5]

[1] *CAS Key Laboratory of Microscale Magnetic Resonance and Department of Modern Physics, University of Science and Technology of China, Hefei, Anhui 230026, China*

[2] *Helmholtz-Institut Mainz, Johannes Gutenberg University, 55128 Mainz, Germany*

[3] *Synergetic Innovation Center of Quantum Information and Quantum Physics, University of Science and Technology of China, Hefei, Anhui 230026, China*

[4] *Synergetic Innovation Center for Quantum Effects and Applications, Hunan Normal University, Changsha, Hunan 410081, China*

[5] *Department of Physics, University of California at Berkeley, California 94720-7300, USA*

(Received 8 August 2018; revised manuscript received 11 November 2018; published 4 February 2019)

Magnetic sensors are important for detecting nuclear magnetization signals in nuclear magnetic resonance (NMR). As a complementary analysis tool to conventional high-field NMR, zero- to ultralow-field (ZULF) NMR detects nuclear magnetization signals in the submicrotesla regime. Current ZULF NMR systems are always equipped with high-quality magnetic shields to ensure that ambient magnetic-field noise does not dwarf the magnetization signal. An alternative approach is to separate the magnetization signal from the noise based on their differing spatial profiles, as can be achieved using a magnetic gradiometer. Here, we present a gradiometric ZULF NMR spectrometer with a magnetic-field-gradient noise of 17 $\mathrm{fT/cm\,Hz^{1/2}}$ in the frequency ranging from 100 to 400 Hz, based on a single vapor cell ($0.7 \times 0.7 \times 1.0$ $\mathrm{cm^3}$). With applied white magnetic-field noise, we show that the gradiometric spectrometer achieves 13-fold enhancement in the signal-to-noise ratio (SNR) compared to the single-channel configuration. By reducing the influence of the common-mode magnetic-field noise, this work enables the use of compact and low-cost magnetic shields. Gradiometric detection also proves to be beneficial for eliminating systematic errors in ZULF-NMR experiments searching for exotic spin-dependent interactions and molecular parity violation.

DOI: 10.1103/PhysRevApplied.11.024005

I. INTRODUCTION

Nuclear magnetic resonance (NMR) is conventionally operated in large magnetic fields and is a powerful analytical technique in chemistry, biology, and medicine [1–3]. As a complementary tool to conventional high-field NMR, zero- and ultralow-field (ZULF) NMR offers improved spectral resolution and untruncated spin interactions [4–9]. Combining with recently developed quantum-control techniques [10–14], ZULF NMR is shown to be promising in probing the frontiers of fundamental physics. For example, the absence of a large applied magnetic field in ZULF NMR allows for the measurement of antisymmetric spin-spin couplings, which are related to chirality [15] and have been proposed as a means for detecting molecular parity nonconservation [16]. Furthermore, ZULF NMR has been recently applied to searches for ultralight dark matter candidates such as axion and axionlike particles [17] and the spin-gravity coupling effect in nucleons [18].

ZULF NMR typically involves low frequencies, so noninductive sensors are necessary for detection. Early ZULF NMR systems used superconducting quantum interference devices (SQUIDs) as magnetic-field sensors [19–22]. One drawback is that SQUIDs must operate under cryogenic conditions. Recent years have seen increased developments in atomic magnetometers, both in sensitivity and portability [23]. A spin-exchange relaxation-free (SERF) atomic magnetometer with a measurement volume of 0.45 $\mathrm{cm^3}$ has a demonstrated sensitivity of 0.16 $\mathrm{fT/Hz^{1/2}}$, comparable to the most advanced SQUIDs [24–26]. The condition for SERF is that the rate of the spin-exchange (SE) collisions greatly exceed the rate of Larmor precession. An individual atom thus precesses only a small angle between collisions. Under this condition, it turns out [27,28] that SE relaxation, a dominant factor that degrades the sensitivity of the atomic magnetometer, is eliminated. In order to have a large SE collision, a cell

*teng@uni-mainz.de
†xhpeng@ustc.edu.cn

with high atomic number density is used and is heated to a temperature above 400 K. A coated cell also opens up the possibility of operating in the SERF regime at low alkali density near room temperature, which is with a coating of sufficient quality that relaxation at the wall is much slower than relaxation due to SE collisions and provides observed T_2 lifetimes as long as 77 s for rubidium at natural abundance [29]. Considering the low-magnetic-field requirement and the high sensitivity, SERF atomic magnetometers have been recently used in ZULF NMR to detect pure J-coupling (indirect spin-spin coupling) spectra at zero field [30,31] and determine the spin-coupling topology at near-zero magnetic field [32,33].

In ZULF NMR, the noise level of a measurement is frequently dominated by the ambient magnetic-field noise. Although such noise can be suppressed with magnetic shields, there is additional magnetic-field noise due to Johnson currents from the shields themselves [34]. There is also magnetic-field noise from heaters, thermistors, and the magnetic nulling coils. To reduce the sensitivity to this noise, we use a gradiometric NMR spectrometer based on a two-channel SERF atomic magnetometer. Important steps toward multichannel magnetometers have been shown [25,26,35,36]. A recent work in Ref. [37] introduced a compact microfabricated magnetic gradiometer that consists of two chip-scale atomic vapor cells, with a demonstrated magnetic-field-gradient noise level of $5\,\mathrm{fT/cm\,Hz^{1/2}}$ at frequencies above 20 Hz (hereafter, we use the root-mean-square value of noise). The method of gradiometric measurement is widely used in other areas such as atom interferometry [38,39] and optical lattice clocks [40]. Considering these already existing achievements in the gradiometric measurement, our work does not focus on further sensitivity enhancement, but instead, on extending the practical applications of this method, specifically, in ZULF-NMR. Compared with previous ZULF-NMR spectrometers, our gradiometric spectrometer is sensitive to the magnetic-field gradient produced by the NMR sample but insensitive to homogeneous magnetic fields. The magnetic-field-gradient noise level is measured to be $17\,\mathrm{fT/cm\,Hz^{1/2}}$, which is less than the typical magnetic-field gradient produced by the NMR samples, e.g., $4\,\mathrm{pT/cm\,Hz^{1/2}}$ for ^{13}C-formic acid in this experiment. By using the gradiometric spectrometer, we demonstrate high signal-to-noise ratio (SNR) measurement of liquid-state NMR samples under the application of spatially homogeneous white magnetic-field noise, with a noise spectral density of approximately $0.3\,\mathrm{pT/Hz^{1/2}}$, comparable to the noise level in an unshielded environment [41,42].

II. EXPERIMENT

The apparatus of the gradiometric spectrometer is shown in Fig. 1, which consists of two basic parts, the NMR sample and the sensor. The NMR sample (approximately

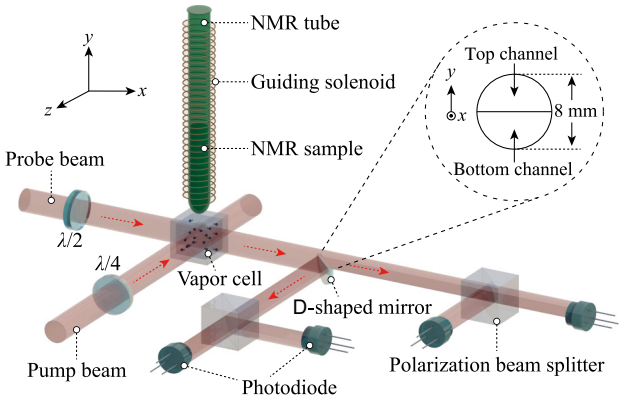

FIG. 1. Schematics of the gradiometric NMR spectrometer. The ^{87}Rb vapor cell is resistively heated to 180°C. A four-layer magnetic shield (not shown) isolates the vapor cell from external magnetic fields. The inset shows that the probe beam (with a $1/e^2$ waist radius of 0.4 cm) is split into top and bottom channels using a D-shaped mirror.

200 μl) in a standard 5-mm glass NMR tube is polarized in a Halbach magnet ($B_p \approx 2.0$ T) for about 30 s, after which the sample is shuttled into the magnetically shielded region, such that the bottom of the sample tube is about 0.3 cm above a ^{87}Rb vapor cell; see Fig. 1. A guiding magnetic field (approximately 3×10^{-4} T) is applied during the transfer and is turned off within 10 μs. Such a suddenly switched-off magnetic field serves effectively as a radio-frequency pulse in conventional high-field NMR. The initial state of the sample at zero field thus remains the high-field equilibrium state and evolves automatically under the J-coupling interaction between nuclear spins, which generates an oscillating magnetization signal and is detected with the sensor [9].

The sensor consists of a ^{87}Rb vapor cell, with an outer dimension of $0.7 \times 0.7 \times 1.0$ cm^3 and a wall thickness of 1 mm. It is more advantageous to use a cell with a rectilinear geometry rather than spherical in this experiment, since for the latter case, the expanded probe beam is distorted and scattered when transmitted through the cell. The cell is optically pumped with a circularly polarized laser beam propagating in the $-z$ direction, of which the frequency is tuned to the center of the buffer-gas (500 torr N_2) broadened and shifted D1 line of ^{87}Rb. The magnetic field is measured via optical rotation of a linearly polarized probe laser beam at the D2 transition propagating in the x direction. The probe beam is expanded to have a $1/e^2$ waist radius of 0.4 cm, which is able to cover the inner area of the vapor cell. After the cell, the probe beam is split into two channels, top and bottom channels, respectively, using a D-shaped mirror. The sensing volume of each channel is about 0.1 cm^3. The inclusion of the buffer gas sets the diffusion length of rubidium atoms in one relaxation time to be about $(DT_2)^{1/2} \approx 0.01$ cm (D is the diffusion constant [43]

and T_2 is the atomic spin relaxation time), which is much smaller than the spatial separation of the two channels (approximately 0.4 cm). As a result, each channel provides a local measurement of the magnetic field. It is worth noting that the rubidium atoms in both channels have the same buffer-gas broadened and shifted resonance profile. This situation is beneficial for canceling some common-mode technical noise, converted from the frequency and intensity noise of the pump beam through the light-shift effect [44].

Gradiometric measurements are performed by subtracting the signals measured with the two channels. In order to perform efficient gradiometric measurements, the responses of the two channels with respect to an oscillating magnetic field need to be calibrated. The difference in the response of the two channels is measured by applying an oscillating y-magnetic field at different frequencies. The oscillating magnetic field is generated through a function generator (DS345, Standford Research Systems), of which the output is fed into a pair of Helmholtz coils (five turns, with a diameter of 7 cm) around the sensor. Figure 2 shows that the phase difference between the two channels is a function of frequency f and can be fitted with $\arctan[f(A-B)/(f^2+A\times B)]$ (see the Supplemental Material for detailed derivations [45]). Here, A and B are the bandwidths for the top and bottom channels, respectively. The fit indicates that $A = 206.9$ Hz and $B = 148.9$ Hz. Since the response of the magnetometer is a function of the pump intensity [46], the difference in the bandwidth is due to the unevenly distributed power of the pump beam in the two channels. The maximum phase difference of approximately 0.16 rad happens when the frequency is $f=\sqrt{A\times B}\approx 175.5$ Hz, which agrees well with the experimental results in Fig. 2. Based on these fitting parameters, we zero the phase difference between the two channels at different frequencies and perform gradiometric measurements.

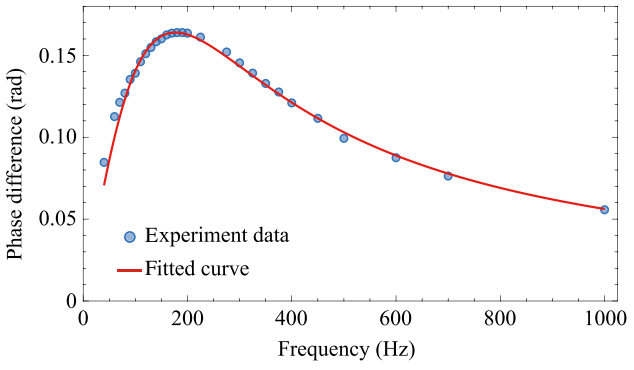

FIG. 2. The dependence of the phase difference between top and bottom channels on frequency. The points (circle) are experimentally measured phase differences through applying an oscillating y-field at different frequencies f. The experimental results are fitted to $\arctan[f(A-B)/(f^2+A\times B)]$ (see Supplemental Material [45]). Here, A and B are the bandwidths for the top and bottom channels, respectively. The fit (red line) indicates $A = 206.9$ Hz and $B = 148.9$ Hz.

III. RESULTS AND DISCUSSION

Figure 3(a) shows the magnetic-field noise of the apparatus. A single channel has a noise floor of about 14 $\mathrm{fT/Hz^{1/2}}$ [see the blue line in Fig. 3(a)], which is dominated by Johnson noise of the shield (Twinleaf MS-1) [34] and the intensity noise of the probe beam. The subtraction of the measured signals from the top and bottom channels, after proper phase and amplitude calibration, gives a noise floor of ~ 7 $\mathrm{fT/Hz^{1/2}}$ [see the black line in Fig. 3(a)]. We also measure the intensity noise of the probe beam under the same conditions except that the pump beam is blocked [see the red line in Fig. 3(a)], which has almost the same level as that of the difference of the two channels. By comparing the probe laser intensity noise and the noise of the difference, we conclude that the probe laser intensity noise shown in Fig. 3(a) is the non-common-mode noise for the two channels. This conclusion is valid considering that the two beams are probed with different photodiodes, propagate along different paths, and experience different fluctuations from the airflow and optical components. Dividing the noise floor of the difference by the spatial separation between the two channels gives the magnetic-field-gradient noise of the gradiometric spectrometer, which is approximately 17 $\mathrm{fT/cm\,Hz^{1/2}}$ from 100 to 400 Hz.

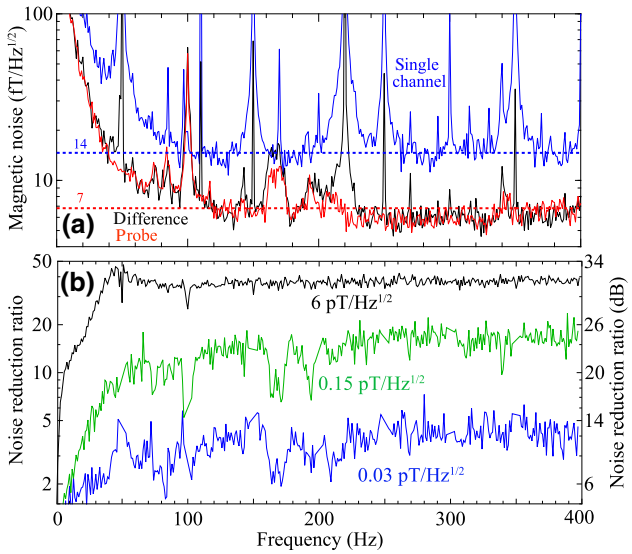

FIG. 3. Magnetic-field noise and the noise reduction ratio of the gradiometric NMR spectrometer. (a) Magnetic-field noise for the single channel (blue line) and the difference of the two channels (black line). The probe-beam intensity noise is measured with the pump beam blocked and is shown with the red line. (b) The noise reduction ratio for the gradiometric NMR spectrometer under the application of white magnetic noise with different amplitudes.

Figure 3(b) shows the noise reduction ratio under the applications of different white magnetic-field noise. The noise reduction ratio is calculated as $N_{\text{single}}(f)/N_{\text{diff}}(f)$, where $N_{\text{single}}(f)$ is the noise level of the single channel and $N_{\text{diff}}(f)$ is the noise level of the difference. We can further expand $N_{\text{single}}(f)$ as $N_{\text{c}}(f)+N_{\text{nc}}(f)$, where $N_{\text{c}}(f)$ is the common-mode noise and $N_{\text{nc}}(f)$ is the non-common-mode noise. The noise level of the difference can be as well rewritten as $kN_{\text{c}}(f)+N_{\text{nc}}(f)$. The parameter k describes the remaining portion of the common-mode noise in the difference, the reciprocal of which is the common-mode noise rejection ratio (CMRR) of the gradiometer. The noise reduction ratio becomes equal to the CMRR if the common-mode noise is much larger than the non-common-mode noise. This result is experimentally verified by measuring the noise reduction ratio under the applications of different white magnetic-field noise; see Fig. 3(b). The white magnetic-field noise is generated from the same function generator and Helmholtz coils introduced in Sec. II. Under the application of large white magnetic-field noise, e.g., 6 $\text{pT}/\text{Hz}^{1/2}$, which is nearly three orders of magnitude larger than the non-common-mode noise (approximately 7 $\text{fT}/\text{Hz}^{1/2}$), the measured noise reduction ratio is about 40 in the high-frequency region. k is thus calculated as about $1/40=0.025$. Based on this, the noise reduction ratios under the applications of 0.15 $\text{pT}/\text{Hz}^{1/2}$ and 0.03 $\text{pT}/\text{Hz}^{1/2}$ white magnetic-field noise are estimated as 15.25 and 5.67, respectively, which are almost the same as the experimentally measured results shown in Fig. 3(b). Furthermore, Fig. 3(b) shows that the noise reduction ratio is a function of frequency. For a white magnetic-field noise with a given amplitude spectral density, e.g., 6 $\text{pT}/\text{Hz}^{1/2}$, the measured noise reduction ratio is around 40 in a frequency range between 40 and 400 Hz; for lower frequencies, the noise reduction ratio is lower than 40 and increases with the frequency. The reduced noise reduction ratio is because of the frequency-dependent non-common-mode noise in the two channels, which is higher at lower frequency; see the black line in Fig. 3(a). Moreover, as mentioned above, the performance of the gradiometric measurement depends on the calibration of the response of the two channels. Since the system is more noisy in the lower-frequency region, the calibration accuracy for the two channels also decreases, see the increased discrepancy between the fitted curve and the measured results in Fig. 2 at low frequencies.

With the gradiometric NMR spectrometer, high-SNR NMR spectroscopy can be achieved even in a noisy environment. ZULF-NMR spectroscopy of thermally polarized samples is discussed in Refs. [32,33]. Compared with high-field NMR, in which the spectroscopy is performed on specific nuclei, the spectroscopy of ZULF-NMR is based on coupled spins. For a typical XA_n system, where X and A are spin-1/2 particles, and each A couples to X with the same strength J, the resulting zero-field J-coupling spectra

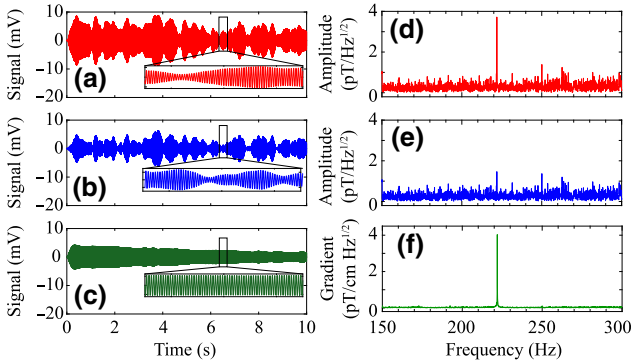

FIG. 4. Single-shot zero-field NMR of ^{13}C-formic acid. White magnetic-field noise is applied though Helmholtz coils along the y direction. The ^{13}C-formic acid time-domain signals are observed in top (a), bottom (b), and gradiometric (c) channels at zero magnetic field, which are filtered with a second-order band-pass filter with cutoff frequencies at 220 and 224 Hz in order to show the oscillating signals clearly. The signals are suppressed at the beginning due to the use of the band-pass filter. The insets in (a)–(c) are enlarged plots of the signal within a time window of 300 ms. (d), (e), and (f) show the frequency-domain signals, which are obtained from the fast Fourier transform (FFT) of the unfiltered original time-domain signals from the three channels.

consist of a single line at J for XA; a single line at $3J/2$ for XA_2; and two lines, one at J and the other at $2J$, for XA_3 [6]. A single-shot NMR signal for ^{13}C-formic acid (H^{13}COOH, from Sigma-Aldrich) obtained with our gradiometric NMR spectrometer is shown in Fig. 4. White magnetic-field noise is applied though the Helmholtz coils along the y direction. The amplitude spectral density of the noise is about 0.3 $\text{pT}/\text{Hz}^{1/2}$. A clear oscillating signal is observed from the gradiometric channel [Fig. 4(c)], compared with the signals in the single channels [Figs. 4(a) and 4(b)]. As shown in Figs. 4(d)–4(f), the fast Fourier transform (FFT) spectra consist of a single line at 221.9 Hz and the signal-to-noise ratios for single shot are 15.1, 6.0, and 202.9 for the top, bottom, and gradiometric channel, respectively. This indicates a 13-fold improvement in the SNR of the gradiometric channel compared with that of the single channel. It is worth noting that the power-line-frequency noise (the harmonics of 50 Hz) are as well suppressed in the gradiometric channel.

The magnetization signals measured by the two channels have a $1/r^3$ dependence, where r is the distance between the channel and the sample. In the current system, the distance between the top (bottom) channel with the sample is 0.85 cm (1.25 cm). Based on this, we estimate that the bottom channel has about 33% of the signal amplitude of the top channel, which agrees well with the measured results; see Figs. 4(d) and 4(e). By slightly increasing the spatial separation of the two channels, e.g., to 10 mm, the signal amplitude of the bottom channel reduces to 10% of the top channel, which might

enhance the SNR of the gradiometric channel. However, there exists a trade-off, since increasing the spatial separation makes the noise from the two channels become less correlated, which can in turn increase the noise level in the gradiometric channel. The optimum spatial separation can be found by changing the probe beam size and measuring the SNR of the gradiometric channel. In order to do this, a larger atomic vapor cell is required.

We also use the gradiometric NMR spectrometer to measure molecules with more complex structures, as shown in Fig. 5. For the XA_3 case, the zero-field NMR spectra of methanol ($^{13}CH_3OH$, from Sigma-Aldrich) is shown in Figs. 5(a)–5(c). Each spectrum is the averaged result from eight transients. Similarly, white magnetic-field noise is applied to the gradiometric NMR spectrometer. The observed signal-to-noise ratios of the peak at 140.5 Hz are 13.7, 7.8, and 68.2 and at 281.1 Hz are 12.9, 5.9, and 82.2 for the top, bottom, and gradiometric channel, respectively. We present a simple rule to identify noisy peaks by comparing their gradient ratios with the expected values. In Figs. 5(a) and 5(b), a dubious line at 117.7 Hz exists in both channels and the amplitude ratio between the top- and bottom-channel signals is nearly 1, which is sufficiently smaller than the expected signal-amplitude ratio of the top and bottom channels. This provides a good-confidence approach to distinguishing lines of spurious origin from NMR signals. Figures 5(d)–5(f) show the partial zero-field spectrum of fully labeled acetonitrile ($^{13}CH_3^{13}C^{15}N$, from Sigma-Aldrich) in the frequency range of 110 to 160 Hz. The full spectrum of $^{13}CH_3^{13}C^{15}N$ is presented in the Supplemental Material [45]. The signal-to-noise ratios of a peak at 131.0 Hz are 23.7, 12.0, and 52.0 for the top, bottom, and gradiometric channel, respectively. The spurious peak at 150 Hz, which is close to one of the NMR peaks, is efficiently suppressed in the gradiometric channel.

Ultralow-field NMR spectroscopy is used for the identification of spin-coupling topology [32,33]. In the presence of a small magnetic field B_z, the degenerate eigenstates of ^{13}C-formic acid split into corresponding manifolds. In Figs. 6(a) and 6(b), the single-shot time-domain NMR signals are perturbed by the ambient magnetic-field noise. However, we observe an obvious beating by using the gradiometric NMR spectrometer, as shown in Fig. 6(c). In Fig. 6(f), a doublet with frequencies $J \pm B_z(\gamma_H + \gamma_C)/2$ is visible with a higher SNR than those in Figs. 6(d) and 6(e). Here, γ_H and γ_C denote the gyromagnetic ratios for proton and carbon nuclear spins, respectively. The frequency splitting of the doublet is measured to be $\Delta = B_z(\gamma_H + \gamma_C) = 1.724(2)$ Hz and then B_z is calculated to be 32.36(4) nT. The full width at half maximum (FWHM) of the single line is around 30 mHz, corresponding to a coherence lifetime of about 10 s. Since the absolute magnetic-field gradient is small in the magnetic shield, the factors that determine the width of the ZULF-NMR signal are the residual magnetic field, intramolecular dipole-dipole interactions, and/or externally fluctuating fields due to paramagnetic impurities (the residual oxygen mixed

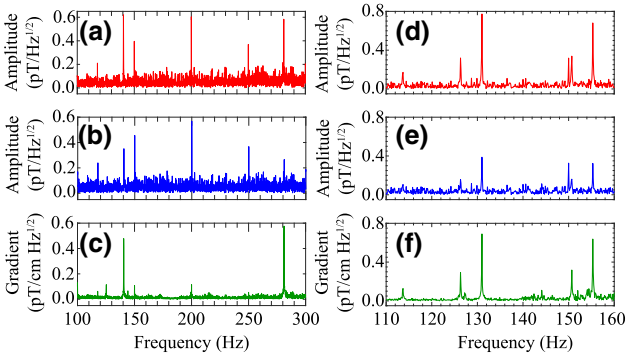

FIG. 5. Zero-field NMR spectra of ^{13}C-methanol (a)–(c) and a portion of the spectra of fully labeled acetonitrile (from 110 to 160 Hz) (d)–(f). Each spectrum is the averaged result from eight transients. White magnetic-field noise is applied though Helmholtz coils along the y direction. At zero magnetic field, the spectra of ^{13}C-methanol ($^{13}CH_3OH$) are observed in the top (a), bottom (b), and gradiometric (c) channels, respectively. The portions of the spectra of fully labeled acetonitrile ($^{13}CH_3^{13}C^{15}N$) are observed in top (d), bottom (e), and gradiometric (f) channels, respectively. Both (c) and (f) show that the gradiometer channel improves the SNR and reduces the spurious lines (the harmonics of 50 Hz). The full spectrum of $^{13}CH_3^{13}C^{15}N$ is shown in the Supplemental Material [45].

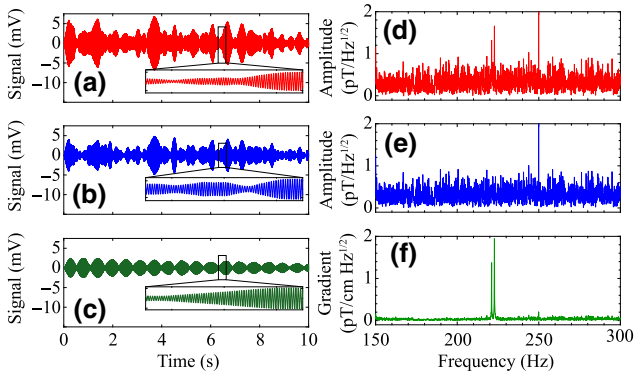

FIG. 6. Single-shot ultralow-field NMR of ^{13}C-formic acid. White magnetic-field noise is applied though Helmholtz coils along the y direction. The ^{13}C-formic acid time-domain signals are observed in top (a), bottom (b), and gradiometric (c) channels in the presence of a small z magnetic field [$B_z \approx 32.36(4)$ nT] and are filtered with a second-order band-pass filter with cutoff frequencies at 220 and 224 Hz in order to show the oscillating signals clearly. The signals are suppressed at the beginning due to the use of the band-pass filter. The insets in (a)–(c) are enlarged plots of the signal within a time window of 300 ms. (d), (e), and (f) show the frequency-domain signals, which are obtained from the FFT of the unfiltered original time-domain signals from the three channels.

with the sample) or other nuclei [47]. Furthermore, it has been experimentally investigated that the linewidth is also a function of the temperature inhomogeneities [48]. In order to see the doublet splitting, the minimum B_z is about 0.6 nT, which gives a splitting of about 30 mHz. We notice that the doublet displays an asymmetry; i.e., the amplitude ratio between peaks at $J \pm B_z(\gamma_H + \gamma_C)/2$ is about $1 : 0.7$. In previous works on ultralow-field NMR using SERF atomic magnetometers [33,49], the asymmetry was also observed in the spectra. Evaluating high-order corrections to the eigenstates, the asymmetry of the doublet is found to be $2\Delta/J \approx 1.5\%$, which is sufficiently smaller than the experimentally observed value (approximately 35%). We found that the asymmetry is due to changes in the sensitive directions in the SERF atomic magnetometers, i.e., the SERF magnetometer is not only sensitive to magnetic signals along the y axis, but simultaneously sensitive to the signals along the x axis when a z-magnetic field is applied (see Supplemental Material [45]).

IV. CONCLUSIONS AND OUTLOOK

We experimentally demonstrate a gradiometric NMR spectrometer with a magnetic-field-gradient noise of $17\,\mathrm{fT/cm\,Hz^{1/2}}$ and a measurement volume for a single channel of 0.1 cm^3. With this device, we demonstrate high SNR NMR spectroscopy in the presence of white magnetic-field noise. This opens the possibility of making a robust and portable NMR spectrometer, particularly in an unshielded environment where large common-mode magnetic-field noise is introduced. Our spectrometer is at an early stage of development and many improvements are possible. For example, we can make the sensor work under the closed-loop operation, as mentioned in Ref. [37], which leads to a better reduction ratio to the common-mode noise. Also, the amplitude of ZULF NMR signals can be maximized by applying suitable magnetic-field excitation pulses [8,30]. With further optimizations, such as decreased probe-beam fluctuations, uniform pump laser power, and optimized spatial separation between the two channels, the gradiometric NMR spectrometer could be capable of detecting NMR signals from samples with natural isotopic abundance for dilute nuclei, which are convenient for chemical analysis. The gradiometric technique is not restricted just to the detection of NMR, but also opens up avenues of investigations of samples that generate magnetic-field gradients, such as magnetic nanoparticles used in biomolecular labeling and cell separation [50–52]. Moreover, recent theoretical work suggests that it is possible to measure molecular chirality and parity nonconservation effects in ZULF NMR [15,16]. Observation of such effects requires an oriented sample that can be obtained by applying a strong electric field, which creates unavoidable magnetic-field noise [53]. An optimized gradiometric spectrometer is promising for sensing such chirality and parity nonconservation effects while remaining robust against background magnetic-field noise.

ACKNOWLEDGMENTS

We acknowledge useful discussions with Dong Sheng on the performance characterizations of the gradiometer. We thank Jiankun Chen for preparing the setup diagram and Georgios Chatzidrosos for fruitful phase-related discussions. This research was supported by the DFG (Deutsche Forschungsgemeinschaft) Koselleck Program and the Heising-Simons and Simons Foundations, the European Research Council under the European Union's Horizon 2020 Research, and Innovative Programme under Grant No. 695405 (T.W., J.W.B., and D.B.). M.J. would like to acknowledge support from the China Scholarship Council (CSC) enabling his research at the Johannes Gutenberg-University Mainz. X.P. acknowledges the support from the National Key Research and Development Program of China (Grant No. 2018YFA0306600); the National Key Basic Research Program of China (Grant No. 2014CB848700); National Natural Science Foundation of China (Grants No. 11425523, No. 11375167, No. 11661161018, and No. 11227901); and Anhui Initiative in Quantum Information Technologies (Grant No. AHY050000).

[1] R. R. Ernst, G. Bodenhausen, and A. Wokaun, *Principles of Nuclear Magnetic Resonance in One and Two Dimensions* (Clarendon Press, Oxford, 1987).

[2] Z. P. Liang and P. C. Lauterbur, *Principles of Magnetic Resonance Imaging: A Signal Processing Perspective* (IEEE Press, Piscataway, 1999).

[3] K. Wüthrich, *NMR of Proteins and Nucleic Acids* (Wiley, New York, 1986).

[4] D. P. Weitekamp, A. Bielecki, D. Zax, K. Zilm, and A. Pines, Zero-field Nuclear Magnetic Resonance, Phys. Rev. Lett. **50**, 1807 (1983).

[5] C. J. Lee, D. Suter, and A. Pines, Theory of multiple-pulse NMR at low and zero fields, J. Magn. Reson. **75**, 110 (1987).

[6] T. Theis, P. Ganssle, G. Kervern, S. Knappe, J. Kitching, M. P. Ledbetter, D. Budker, and A. Pines, Parahydrogen-enhanced zero-field nuclear magnetic resonance, Nat. Phys. **7**, 571 (2011).

[7] J. W. Blanchard, T. F. Sjolander, J. P. King, M. P. Ledbetter, E. H. Levine, V. S. Bajaj, D. Budker, and A. Pines, Measurement of untruncated nuclear spin interactions via zero- to ultralow-field nuclear magnetic resonance, Phys. Rev. B **92**, 220202 (2015).

[8] J. W. Blanchard and D. Budker, Zero- to ultralow-field NMR, eMagRes **5**, 1395 (2016).

[9] M. C. D. Tayler, T. Theis, T. F. Sjolander, J. W. Blanchard, A. Kentner, S. Pustelny, A. Pines, and D. Budker, Instrumentation for nuclear magnetic resonance in zero and

ultralow magnetic field, Rev. Sci. Instrum. **88**, 091101 (2017).
[10] T. F. Sjolander, M. C. D. Tayler, J. P. King, D. Budker, and A. Pines, Transition-selective pulses in zero-field nuclear magnetic resonance, J. Phys. Chem. A **120**, 4343 (2016).
[11] M. C. D. Tayler, T. F. Sjolander, A. Pines, and D. Budker, Nuclear magnetic resonance at millitesla fields using a zero-field spectrometer, J. Magn. Reson. **270**, 35 (2016).
[12] T. F. Sjolander, M. C. D. Tayler, A. Kentner, D. Budker, and A. Pines, ^{13}C-Decoupled J-coupling spectroscopy using two-dimensional nuclear magnetic resonance at zero-field, J. Phys. Chem. Lett. **8**, 1512 (2017).
[13] J. Bian, M. Jiang, J. Cui, X. Liu, B. Chen, Y. Ji, B. Zhang, J. W. Blanchard, X. Peng, and J. Du, Universal quantum control in zero-field nuclear magnetic resonance, Phys. Rev. A **95**, 052342 (2017).
[14] M. Jiang, T. Wu, J. W. Blanchard, G. Feng, X. Peng, and D. Budker, Experimental benchmarking of quantum control in zero-field nuclear magnetic resonance, Sci. Adv. **4**, eaar6327 (2018).
[15] J. P. King, T. F. Sjolander, and J. W. Blanchard, Antisymmetric couplings enable direct observation of chirality in nuclear magnetic resonance spectroscopy, J. Phys. Chem. Lett. **8**, 710 (2017).
[16] J. P. King, T. F. Sjolander, J. W. Blanchard, M. G. Kozlov, and D. Budker, Parity nononserving nuclear spin coupling in molecules, arXiv:1710.06819 (2017).
[17] A. Garcon *et al.*, The cosmic axion spin precession experiment (CASPEr): A dark-matter search with nuclear magnetic resonance, Quantum Sci. Technol. **3**, 014008 (2017).
[18] T. Wu, J. W. Blanchard, D. F. Kimball, M. Jiang, and D. Budker, Nuclear-spin Comagnetometer Based on a Liquid of Identical Molecules, Phys. Rev. Lett. **121**, 023202 (2018).
[19] Y. S. Greenberg, Application of superconducting quantum interference devices to nuclear magnetic resonance, Rev. Mod. Phys. **70**, 175 (1998).
[20] R. McDermott, A. H. Trabesinger, M. Mück, E. L. Hahn, A. Pines, and J. Clarke, Liquid-state NMR and scalar couplings in microtesla magnetic fields, Science **22**, 2247 (2002).
[21] M. Burghoff, S. Hartwig, L. Trahms, and J. Bernarding, Nuclear magnetic resonance in the nanoTesla range, Appl. Phys. Lett. **87**, 054103 (2005).
[22] J. H. Storm, P. Hömmen, D. Drung, and R. Körber, An ultra-sensitive and wideband magnetometer based on a superconducting quantum interference device, Appl. Phys. Lett. **110**, 072603 (2017).
[23] D. Budker and M. V. Romalis, Optical magnetometry, Nat. Phys. **3**, 227 (2007).
[24] J. C. Allred, R. N. Lyman, T. W. Kornack, and M. V. Romalis, High-sensitivity Atomic Magnetometer Unaffected by Spin-exchange Relaxation, Phys. Rev. Lett. **89**, 130801 (2002).
[25] I. K. Kominis, T. W. Kornack, J. C. Allred, and M. V. Romalis, A subfemtotesla multichannel atomic magnetometer, Nature **422**, 596 (2003).
[26] H. B. Dang, A. C. Maloof, and M. V. Romalis, Ultrahigh sensitivity magnetic field and magnetization measurements with an atomic magnetometer, Appl. Phys. Lett. **97**, 151110 (2010).
[27] W. Happer and H. Tang, Spin-exchange Shift and Narrowing of Magnetic Resonance Lines in Optically Pumped Alkali Vapors, Phys. Rev. Lett. **31**, 273 (1973).
[28] W. Happer and A. C. Tam, Effect of rapid spin exchange on the magnetic-resonance spectrum of alkali vapors, Phys. Rev. A **16**, 1877 (1977).
[29] M. V. Balabas, T. Karaulanov, M. P. Ledbetter, and D. Budker, Polarized Alkali-metal Vapor with Minute-long Transverse Spin-relaxation Time, Phys. Rev. Lett. **105**, 070801 (2010).
[30] M. P. Ledbetter, C. W. Crawford, A. Pines, D. E. Wemmer, S. Knappe, J. Kitching, and D. Budker, Optical detection of NMR J-spectra at zero magnetic field, J. Magn. Reson. **199**, 25 (2009).
[31] J. W. Blanchard, M. P. Ledbetter, T. Theis, M. C. Butler, D. Budker, and A. Pines, High-resolution zero-field NMR J-spectroscopy of aromatic compounds, J. Am. Chem. Soc. **135**, 3607 (2013).
[32] S. Appelt, F. W. Häsing, U. Sieling, A. Gordji-Nejad, S. Glöggler, and B. Blümich, Paths from weak to strong coupling in NMR, Phys. Rev. A **81**, 023420 (2010).
[33] M. P. Ledbetter, T. Theis, J. W. Blanchard, H. Ring, P. Ganssle, S. Appelt, B. Blümich, A. Pines, and D. Budker, Near-zero-field Nuclear Magnetic Resonance, Phys. Rev. Lett. **107**, 107601 (2011).
[34] J. Nenonen, J. Montonen, and T. Katila, Thermal noise in biomagnetic measurements, Rev. Sci. Instrum. **67**, 2397 (1996).
[35] R. Wyllie, M. Kauer, R. T. Wakai, and T. G. Walker, Optical magnetometer array for fetal magnetocardiography, Opt. Lett. **37**, 2247 (2012).
[36] J. Fang, T. Wang, W. Quan, H. Yuan, H. Zhang, Y. Li, and S. Zou, *In situ* magnetic compensation for potassium spin-exchange relaxation-free magnetometer considering probe beam pumping effect, Rev. Sci. Instrum. **85**, 063108 (2014).
[37] D. Sheng, A. R. Perry, S. P. Krzyzewski, S. Geller, J. Kitching, and S. Knappe, A microfabricated optically-pumped magnetic gradiometer, Appl. Phys. Lett. **110**, 031106 (2017).
[38] M. J. Snadden, J. M. McGuirk, P. Bouyer, K. G. Haritos, and M. A. Kasevich, Measurement of the Earth's Gravity Gradient with an Atom Interferometer-based Gravity Gradiometer, Phys. Rev. Lett. **81**, 971 (1998).
[39] F. Sorrentino, A. Bertoldi, Q. Bodart, L. Cacciapuoti, M. de Angelis, Y.-H. Lien, M. Prevedelli, G. Rosi, and G. M. Tino, Simultaneous measurement of gravity acceleration and gravity gradient with an atom interferometer, Appl. Phys. Lett. **101**, 114106 (2012).
[40] G. E. Marti, R. B. Hutson, A. Goban, S. L. Campbell, N. Poli, and J. Ye, Imaging Optical Frequencies with 100 μHz Precision and 1.1 μm Resolution, Phys. Rev. Lett. **120**, 103201 (2018).
[41] G. Bevilacqua, V. Biancalana, A. B. Baranga, Y. Dancheva, and C. Rossi, Microtesla NMR J-coupling spectroscopy with an unshielded atomic magnetometer, J. Magn. Reson. **263**, 65 (2016).
[42] S. J. Seltzer and M. V. Romalis, Unshielded three-axis vector operation of a spin-exchange-relaxation-free atomic magnetometer, Appl. Phys. Lett. **85**, 4804 (2004).

[43] F. A. Franz and C. Volk, Spin relaxation of rubidium atoms in sudden and quasimolecular collisions with light-noble-gas atoms, Phys. Rev. A **14**, 1711 (1976).
[44] T. Wu, X. Peng, and H. Guo, Light shift manipulation and suppression in a double pass optical-magnetic double resonance system, Laser Phys. **24**, 106001 (2014).
[45] See Supplemental Material at http://link.aps.org/supplemental/10.1103/PhysRevApplied.11.024005 for details of the calculations and experiments.
[46] M. P. Ledbetter, I. M. Savukov, V. M. Acosta, D. Budker, and M. V. Romalis, Spin-exchange-relaxation-free magnetometry with Cs vapor, Phys. Rev. A **77**, 033408 (2008).
[47] M. Carravetta and M. H. Levitt, Theory of long-lived nuclear spin states in solution nuclear magnetic resonance. I. Singlet states in low magnetic field, J. Chem. Phys. **122**, 214505 (2005).
[48] M. Emondts, M. P. Ledbetter, S. Pustelny, T. Theis, B. Patton, J. W. Blanchard, M. C. Butler, D. Budker, and A. Pines, Long-lived Heteronuclear Spin-singlet States in Liquids at a Zero Magnetic Field, Phys. Rev. Lett. **112**, 077601 (2014).
[49] M. P. Ledbetter, S. Pustelny, D. Budker, M. V. Romalis, J. W. Blanchard, and A. Pines, Liquid-state Nuclear Spin Comagnetometers, Phys. Rev. Lett. **108**, 243001 (2012).
[50] B. Gleich and J. Weizenecker, Tomographic imaging using the nonlinear response of magnetic particles, Nature **435**, 1214 (2005).
[51] D. Yu, S. Ruangchaithaweesuk, L. Yao, and S. Xu, Detecting molecules and cells labeled with magnetic particles using an atomic magnetometer, J. Nanopart. Res. **14**, 1135 (2012).
[52] L. Bougas, L. D. Langenegger, C. A. Mora, M. Zeltner, W. J. Stark, A. Wickenbrock, J. W. Blanchard, and D. Budker, Nondestructive in-line sub-picomolar detection of magnetic nanoparticles in flowing complex fluids, Sci. Rep. **8**, 3491 (2018).
[53] M. V. Romalis, W. C. Griffith, J. P. Jacobs, and E. N. Fortson, New Limit on the Permanent Electric Dipole Moment of ^{199}Hg, Phys. Rev. Lett. **86**, 2505 (2001).